



# Influence of Orbit and Mass Constraints on Reflected Light Characterization of Directly Imaged Rocky Exoplanets

Arnaud Salvador<sup>1,2,3,4</sup> , Tyler D. Robinson<sup>1,2,3,4</sup> , Jonathan J. Fortney<sup>5</sup> , and Mark S. Marley<sup>1</sup>

<sup>1</sup>Lunar & Planetary Laboratory, University of Arizona, Tucson, AZ 85721, USA; [arnaudsalvador@arizona.edu](mailto:arnaudsalvador@arizona.edu)

<sup>2</sup>Department of Astronomy and Planetary Science, Northern Arizona University, Flagstaff, AZ 86011, USA

<sup>3</sup>Habitability, Atmospheres, and Biosignatures Laboratory, University of Arizona, Tucson, AZ 85721, USA

<sup>4</sup>NASA Nexus for Exoplanet System Science Virtual Planetary Laboratory, University of Washington, Box 351580, Seattle, WA 98195, USA

<sup>5</sup>Department of Astronomy and Astrophysics, University of California, Santa Cruz, CA 95064, USA

Received 2024 February 13; revised 2024 May 30; accepted 2024 June 5; published 2024 July 1

## Abstract

Survey strategies for upcoming exoplanet direct imaging missions have considered varying assumptions of prior knowledge. Precursor radial velocity surveys could have detected nearby exo-Earths and provided prior orbit and mass constraints. Alternatively, a direct imaging mission performing astrometry could yield constraints on the orbit and phase angle of target planets. Understanding the impact of prior mass and orbit information on planetary characterization is crucial for efficiently recognizing habitable exoplanets. To address this question, we use a reflected-light retrieval tool to infer the atmospheric and bulk properties of directly imaged Earth-analogs while considering varying levels of prior information and signal-to-noise ratio (S/N). Because of the strong correlation between the orbit-related parameters and the planetary radius, prior information on the orbital distance and planetary phase angle yield much tighter constraints on the planetary radius: from  $R_p = 2.95_{-1.95}^{+2.69} R_\oplus$  without prior knowledge, to  $R_p = 1.01_{-0.19}^{+0.33} R_\oplus$  with prior determination of the orbit for S/N = 20 in the visible/near-infrared spectral range, thus allowing size determination from reflected light observations. However, additional knowledge of planet mass does not notably enhance radius ( $R_p = 0.98_{-0.14}^{+0.17} R_\oplus$ ) or atmospheric characterization. Also, prior knowledge of the mass alone does not yield a tight radius constraint ( $R_p = 1.64_{-0.80}^{+1.29} R_\oplus$ ) nor improves atmospheric composition inference. By contrast, because of its sensitivity to gas column abundance, detecting a Rayleigh scattering slope or bounding Rayleigh opacity helps to refine gas mixing ratio inferences without requiring prior mass knowledge. Overall, apart from radius determination, increasing the S/N is more beneficial than additional prior observations.

*Unified Astronomy Thesaurus concepts:* Exoplanets (498); Direct imaging (387); Exoplanet atmospheres (487); Astrobiology (74); Biosignatures (2018); Bayesian statistics (1900); Habitable planets (695)

## 1. Introduction

The discovery and characterization of habitable exoplanets (i.e., planets that can maintain stable liquid water on their surface; e.g., Kasting et al. 1993) has been defined as one of the leading decadal goals for astronomy, planetary science, and astrobiology (National Academies of Sciences, Engineering, & Medicine 2023a, 2023b). The so-called Habitable Worlds Observatory (HWO) mission concept is being developed by NASA to help achieve this profound goal. Importantly, HWO builds on the successes of earlier space-based direct imaging concept missions, such as the Habitable Exoplanet Observatory (HabEx; Gaudi et al. 2018, 2020) and the Large Ultraviolet/Optical/Infrared Surveyor (LUVOIR; Roberge & Moustakas 2018; The LUVOIR Team 2019). A coronagraph demonstration as part of the soon-to-launch NASA Nancy Grace Roman Space Telescope will also provide key insights into space-based exoplanet high-contrast imaging techniques (Akeson et al. 2019; Mennesson et al. 2020).

Leveraging recent advances in coronagraph (Trauger & Traub 2007) or starshade (Harness et al. 2021) starlight suppression techniques, HWO is expected to achieve sufficient

planet-star flux contrast for exo-Earth direct imaging (below  $\sim 10^{-10}$  in the visible for an Earth-like planet orbiting a Sun-like star at 1 au; e.g., Guyon et al. 2006; Seager & Deming 2010). Compared to transit spectroscopy, HWO reflected light observation capabilities will probe planets with larger orbital separations from the star and smaller planet-to-star radius ratios (e.g., Madhusudhan 2019). It will also be sensitive to deeper atmospheric layers (up to the surface or the pressure at which aerosols become optically thick; Morley et al. 2015) and even surface conditions (including the detection of oceans' glint; Williams & Gaidos 2008; Robinson et al. 2010). Yet, observations will remain challenging to interpret, and retrieving the atmospheric and surface properties encoded in noisy reflected light spectra will not be straightforward. First and obviously, technical limitations exist (e.g., Juanola-Parramon et al. 2022); the instrument performance and the observation time restrict the spectral coverage and signal-to-noise ratio (S/N) needed to sense spectral signatures (e.g., Feng et al. 2018; Konrad et al. 2022; Damiano & Hu 2022; Alei et al. 2022a; Robinson & Salvador 2023; Susemehl et al. 2023; Latouf et al. 2023a, 2023b; Young et al. 2024). Then, spectral interpretation is challenged by the complexity and our understanding of atmospheric processes (e.g., Seager & Deming 2010), necessarily modeled via simplified parameterizations (e.g., Fortney et al. 2021; Alei et al. 2022b), and the extremely large range of unconstrained parameters (e.g., Madhusudhan 2018). In addition, many degeneracies exist



Original content from this work may be used under the terms of the [Creative Commons Attribution 4.0 licence](#). Any further distribution of this work must maintain attribution to the author(s) and the title of the work, journal citation and DOI.

between these parameters, and disentangling their respective influence is difficult (e.g., Benneke & Seager 2013; Lupu et al. 2016; Nayak et al. 2017; Welbanks & Madhusudhan 2019; Wang et al. 2022). Indeed, solutions are not unique and many combinations of parameters corresponding to different atmospheric states may satisfactorily reproduce a given observed spectrum.

Some of these observational and theoretical shortcomings are addressed by atmospheric retrieval models, that are used to infer the free/unknown parameters that best reproduce/explain current or future noisy exoplanet observations (e.g., Madhusudhan 2018). Recently, and as jointly done for transmission (e.g., Benneke & Seager 2012; Greene et al. 2016; Lustig-Yaeger et al. 2023) and emission spectroscopy (e.g., von Paris et al. 2013; Konrad et al. 2022; Alei et al. 2022a; Mettler et al. 2024), several retrieval studies have assessed the science returns associated with future direct imaging mission designs targeting planets from gas giants and icy planets (Lupu et al. 2016; Nayak et al. 2017; Lacy et al. 2019; Damiano & Hu 2020; Carrión-González et al. 2020; Damiano et al. 2020; Carrión-González et al. 2021; Damiano & Hu 2021; Susemehl et al. 2023) to rocky planets (Feng et al. 2018; Smith et al. 2020; Damiano & Hu 2022; Robinson & Salvador 2023; Susemehl et al. 2023; Damiano et al. 2023; Latouf et al. 2023a, 2023b; Young et al. 2024). In particular, they provide the requirements—in terms of spectral coverage, resolution, and S/N—to confidently identify selected atmospheric and surface properties. Thus, atmospheric retrieval modeling can connect our understanding of how well a direct imaging mission can characterize exoplanetary atmospheres to the underlying observational performance delivered by a mission architecture.

Despite these efforts, the most efficient path to characterizing worlds in reflected light is uncertain, especially with regard to the role of prior observations. Importantly, it has been stated that “knowledge of a planet’s mass (along with a knowledge of its radius) is essential [...] to interpret spectroscopic features in its atmosphere” (National Academies of Sciences Engineering & Medicine 2018). Yet, this assumption has never been confirmed with retrieval models, nor the values of prior mass knowledge quantitatively assessed. Extreme precision radial velocity (EPRV) could provide prior detections of exo-Earths, which changes the demands on any discovery survey (Stark et al. 2019; Dulz et al. 2020; Morgan et al. 2021) while yielding orbit and (minimum) mass measurements (e.g., Lovis et al. 2010; Plavchan et al. 2015). Without EPRV, discovery and characterization require multiple photometric visits, to first find and select the most promising targets for a follow-up in-depth characterization campaign (e.g., Figure 1.5 from The LUVOIR Team 2019). In such a case, the orbit would be determined early to ensure a planet is in its host star’s habitable zone. Alternatively, particularly exciting targets could get marked for spectral observations even before full orbit fits are achieved. Thus, it is important to understand how atmospheric characterization is influenced by prior knowledge of the orbit and/or mass.

Here, we investigate how orbit-related and mass prior information will affect our ability to retrieve other atmospheric and planetary properties and help exoplanet characterization. In Section 2, we describe the retrieval framework and scenarios we considered. Our results showcasing how different levels of prior information at various S/Ns can improve exoplanet

characterization are presented in Section 3. The main conclusions are summarized in Section 4.

## 2. Methods

We use the `rfast` atmospheric retrieval suite (Robinson & Salvador 2023) to assess how prior knowledge of the orbit and mass influence the characterization of an Earth-like exoplanet observed with a typical HWO setup. The model consists of several interconnected tools. First, a radiative transfer “forward” model that generates a synthetic high-resolution spectrum of a planet of known (fiducial) properties. An instrument model then degrades the spectral resolution and adds noise to mimic the “faux observation” for a given instrument/telescope design. A Bayesian sampling tool (`emcee`; Foreman-Mackey et al. 2013) then explores the parameter space of all unknown atmospheric and planetary parameters adopted to fit the faux observation. The set of fit parameters is fed to the forward model that generates the corresponding high-resolution spectrum, which is degraded via the instrument model to match the resolution of the simulated data. The likelihood of the generated spectrum to reproduce the faux observations is computed using the standard definition of chi-squared ( $\chi^2$ ) while the posterior probability informs how the parameter space should be further explored and is computed via Bayes’ theorem. After a burn-in period, the walker positions map the posterior probability distribution. This distribution quantifies which parameter values are most likely to reproduce the simulated observation. Combined with any biases away from the input parameters, this reveals how effectively (or ineffectively) HWO observations could constrain key properties of a directly imaged world. Forward and inverse model validations for `rfast` are presented in Robinson & Salvador (2023).

In high-contrast imaging, the light from the host star that is reflected by the planet is resolved from its bright host as a distinct point source, such that the exoplanet itself is directly imaged. At a given planet–star–observer phase angle,  $\alpha$ , the relevant measure is the wavelength-dependent planet-to-star flux ratio:

$$\frac{F_p}{F_s} = A_g \Phi(\alpha) \left( \frac{R_p}{a} \right)^2, \quad (1)$$

where  $A_g$  is the geometric albedo,  $\Phi$  is the phase function (which depends on the phase angle),  $R_p$  is the radius of the planet, and  $a$  is the orbital distance. While the planet–star angular separation, the host star apparent magnitude, the exozodiacal dust brightness, and other parameters impact the feasibility of the observation, the planet-to-star flux ratio roughly sets the contrast that must be achieved to image the planet. To account for the dependence of the reflected light spectrum on the planetary phase, we use `rfast` 3D mode. The planet is then treated as a homogeneous pixelated globe, where radiative transfer is computed for each pixel following a local plane-parallel assumption. The plane-parallel facets then have different pairs of incidence and emergence angles, depending on the illumination geometry. The total emergent flux from the planet (i.e., from the spatially integrated disk) composed of these many plane-parallel facets is obtained using a Gauss–Chebyshev integration following Horak & Little (1965; see Robinson & Salvador 2023, for more details).

**Table 1**  
Retrieved Parameters, Corresponding Description, Earth-based Fiducial Input Value, and Prior Ranges

Parameter	Description	Input	Flat Prior	Gaussian Prior <sup>c</sup>
<i>Surface Conditions</i>				
$\log p_{\text{surf}}$	Surface pressure (Pa)	$\log(10^5)$	[0, 8]	...
$T$	Atmospheric temperature <sup>a</sup> (K)	255	[100, 1000]	...
$\log A_{\text{surf}}$	Surface albedo	$\log(0.05)$	[-2, 0]	...
<i>Gas Abundances<sup>b</sup></i>				
$\log f_{\text{N}_2}$	Molecular nitrogen mixing ratio	$\log(0.78)$	[-10, 0]	...
$\log f_{\text{O}_2}$	Molecular oxygen mixing ratio	$\log(0.21)$	[-10, 0]	...
$\log f_{\text{H}_2\text{O}}$	Water vapor mixing ratio	$\log(3 \times 10^{-3})$	[-10, 0]	...
$\log f_{\text{CO}_2}$	Carbon dioxide mixing ratio	$\log(4 \times 10^{-4})$	[-10, 0]	...
$\log f_{\text{CH}_4}$	Methane mixing ratio	$\log(2 \times 10^{-6})$	[-10, 0]	...
$\log f_{\text{O}_3}$	Ozone mixing ratio	$\log(7 \times 10^{-7})$	[-10, -2]	...
<i>Cloud Parameters</i>				
$\log p_c$	Cloud-top pressure (Pa)	$\log(6 \times 10^4)$	[0, 8]	...
$\log \Delta p_c$	Cloud thickness (Pa)	$\log(10^4)$	[0, 8]	...
$\log \tau_c$	Cloud optical depth	$\log(10)$	[-3, 3]	...
$\log f_c$	Cloudiness fraction	$\log(0.5)$	[-3, 0]	...
<i>Planetary Bulk Parameters</i>				
$\log R_p$	Planet radius ( $R_{\oplus}$ )	$\log(1)$	[-1, 1]	...
$\log M_p$	Planet mass ( $M_{\oplus}$ )	$\log(1)$	[-1, 2]	{1, 0.1}
<i>Orbital Parameters</i>				
$a$	Planetary orbital distance (au)	1	[0.1, 10]	{1, 0.1}
$\alpha$	Planetary phase angle (°)	90	[0, 180]	{90, 9}

**Notes.**<sup>a</sup> Isothermal atmosphere temperature.<sup>b</sup> The remaining atmosphere is backfilled with argon.<sup>c</sup> Parameters constrained to 10% of Earth's value when considering prior observations. The prior distribution is then a Gaussian  $\{\mu, \sigma\}$  of mean  $\mu$  centered on Earth's value, with a standard deviation  $\sigma$  of 10% the truth value.

Because our focus is on the characterization of Earth-like habitable planets with future direct imaging mission concepts, we simulated the reflected light spectrum of the best characterized habitable planet: Earth. Our fiducial parameter values used to generate these synthetic observations are given in Table 1, where the atmosphere is made primarily of nitrogen (78%) and oxygen (21%), with water vapor, carbon dioxide, methane, ozone, and argon as additional trace species. The Earth analog simulated spectrum is passed to a simple instrument model (Robinson et al. 2016) to mimic observations relevant to HWO (Figure 1).

The `rfast` inverse tool has been designed for the rapid exploration of many atmospheric and planetary parameters without being computationally prohibitive. Here we retrieved on 17 parameters (listed in Table 1 with the input value and prior range considered) whose contributions are encoded in the spectrum. The surface conditions are described via the surface pressure ( $p_{\text{surf}}$ ), the isothermal atmospheric temperature ( $T$ ), and the gray surface albedo ( $A_{\text{surf}}$ ). The atmospheric composition is set by the gas abundances of  $\text{N}_2$ ,  $\text{O}_2$ ,  $\text{H}_2\text{O}$ ,  $\text{CO}_2$ ,  $\text{CH}_4$ , and  $\text{O}_3$  (expressed in terms of atmospheric volume mixing ratios,  $f$ ), where argon fulfills the rest of the atmosphere when the sum of their volume mixing ratios is lower than one. The properties of clouds are captured by their top pressure ( $p_c$ ), thickness ( $\Delta p_c$ ), optical depth ( $\tau_c$ ), and the cloudiness fraction ( $f_c$ ). The planetary bulk parameters are the planet radius ( $R_p$ ) and mass ( $M_p$ ). Finally, the orbit-related parameters are the orbital distance ( $a$ ) and the planet-star–observer phase angle ( $\alpha$ ). `emcee` was run with 15 Markov Chain Monte Carlo

chains (walkers) per parameter (for a total of 255 walkers). For each case, we let `emcee` explore the parameter space for 100,000 steps. Sensitivity studies conducted while developing `rfast` demonstrated that the chains have then fully converged for all retrieved parameters (Robinson & Salvador 2023). Drawing the posterior distributions from the last 5000 steps gives a sufficiently large sample to be statistically representative without being computationally prohibitive. It also maintains consistency with Feng et al. (2018) and Robinson & Salvador (2023) and ensures that the walkers have properly explored the parameter space and forgotten their initial position.

To assess the influence of orbital and mass prior information on exoplanet characterization, we consider three different retrieval scenarios associated with different levels of prior constraints: (1) “no prior constraint,” i.e., none of the retrieved parameters is known a priori; (2) “known orbit,” where a prior determination of the orbit of the planet would give constraints on the orbital distance ( $a$ ) and planetary phase angle ( $\alpha$ ) at the time of observation such that these are constrained to 10% of Earth's value (consistent with HabEx/LUVOIR/HWO astrometry target performance; e.g., Guyon et al. 2013; Horning et al. 2019; The LUVOIR Team 2019; Gaudi et al. 2020); (3) “known orbit and mass,” where both the orbit-related parameters ( $a, \alpha$ ) and the mass of the planet ( $M_p$ ) have been previously informed and are all constrained to 10% of Earth's value (consistent with predicted precision radial velocity semiamplitude uncertainties of 10%; Plavchan et al. 2015). An additional “mass constrained” case, where only the mass is

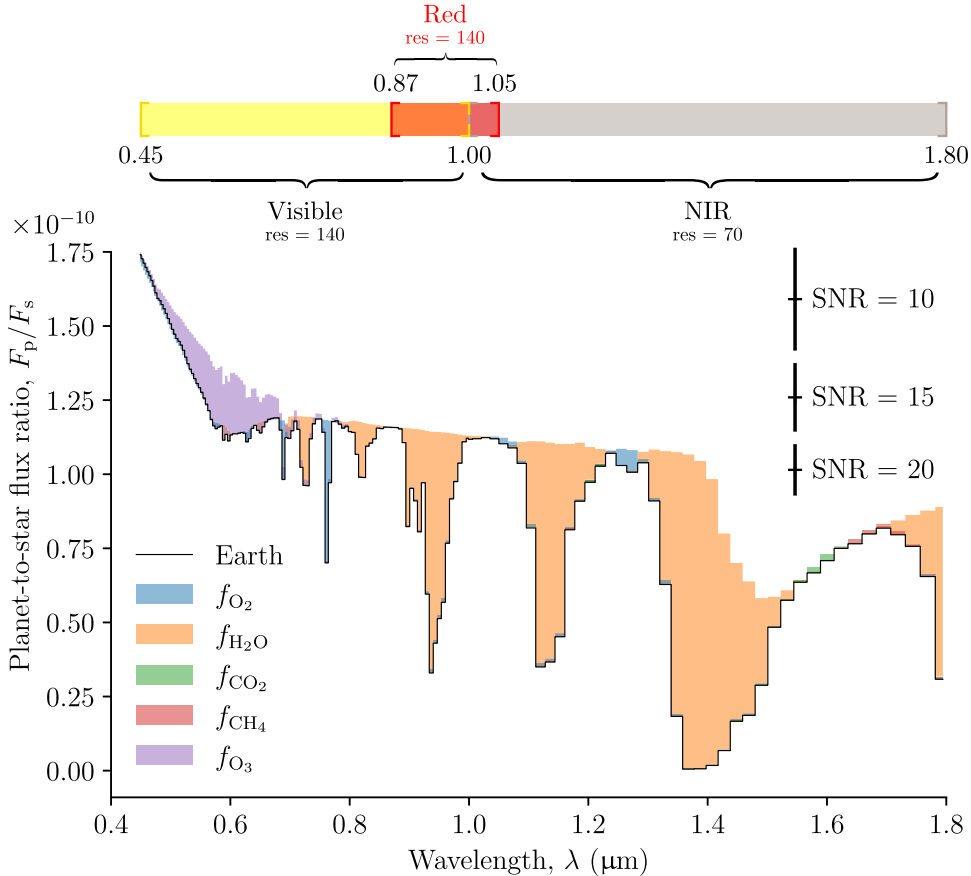


**Figure 1.** Fiducial-model-generated (synthetic) reflected light spectrum of an Earth-like planet at quadrature (i.e., at a planetary phase angle  $\alpha = 90^\circ$ ; see Table 1 for fiducial input values). The colored areas indicate the spectral impact of the gas species by showing the difference between the baseline spectrum (black line) and the spectrum obtained if they were absent from the atmosphere. The top of the figure shows the two wavelength ranges considered and their spectral resolving power: red bandpass ( $\lambda = [0.87, 1.05] \mu\text{m}$ , res = 140; see Appendix B) and visible ( $\lambda = [0.45, 1] \mu\text{m}$ , res = 140) + NIR ( $\lambda = [1, 1.80] \mu\text{m}$ , res = 70). The error bars show the nonrandomized, wavelength-independent noise corresponding to specific S/N at the reference wavelengths  $\lambda = 0.45 \mu\text{m}$  for the vNIR range, and  $\lambda = 0.88 \mu\text{m}$  for the red bandpass.

constrained by prior information, is also shown for a single value of S/N (20) and our baseline spectral coverage (visible/near-infrared; vNIR) to isolate the influence of mass prior determination. Priors are taken as Gaussian constraints. The “known orbit” case models a scenario where the observatory has used earlier observations to help astrometrically constrain the orbit, while the “known orbit and mass” case mimics a scenario where precision radial velocity or astrometric data has obtained an earlier mass determination. Note that none of the scenarios assume any specific mass-radius relationship. Adopting such a relationship as a prior could help to further limit the allowable phase space.

Our instrument model reproduces the observational capabilities of a typical HWO setup operating in the “vNIR” spectral range: an optimistic combination of “visible” ( $\lambda = [0.45, 1] \mu\text{m}$ , with a spectral resolving power  $\text{res} = \lambda/\delta\lambda = 140$ ) and near-infrared (NIR;  $\lambda = [1, 1.80] \mu\text{m}$ ,  $\text{res} = 70$ ) wavelengths (as could be obtained with multiple starshades and/or coronagraph pointings; Figure 1). While it seems reasonable to expect observations spanning the full vNIR bandpass to maximize the yield at the stage of detailed exoplanet characterization, we also tested how our results would apply to observations conducted in a “red” ( $\lambda = [0.87, 1.05] \mu\text{m}$ ,  $\text{res} = 140$ ) coronagraph-restricted bandpass including the prominent  $0.94 \mu\text{m}$   $H_2O$  absorption feature (Figure 1).

For the vNIR baseline spectral coverage, we consider a constant, nonrandomized, gray (i.e., wavelength-independent) noise for three different S/N values (10, 15, and 20) to account for different data quality without being restricted to specific observing parameters such as telescope diameter or target distance (compared to integration times; see Feng et al. 2018). Note that for a constant noise, the S/N goes down within spectral features. The S/N values of 10, 15, or 20 refer to the S/N set at  $\lambda = 0.45 \mu\text{m}$ , which is then propagated across the entire spectral coverage while maintaining a constant error bar size. For the pessimistic red bandpass test, we consider S/N = 10 only (specified at  $0.88 \mu\text{m}$ ). This nonrandomized (i.e., the error bars are simply centered on truth/noise-free values), wavelength-independent noise model follows the approach described in Feng et al. (2018) for their initial validation. Feng et al. (2018) demonstrated that for a statistical sampling of retrievals, a more realistic, randomized noise would yield similar inference results. Furthermore, a constant noise aligns with the predicted performance of the HabEx and LUVOIR missions, assuming equal exposure times across their UV, optical, and NIR spectral bands (The LUVOIR Team 2019; Gaudi et al. 2020). The gray noise approach also enables easier reproducibility, as the wavelength-dependent noise need not be specified. Note that we will specifically address the influence of the data quality (both in terms of spectral coverage

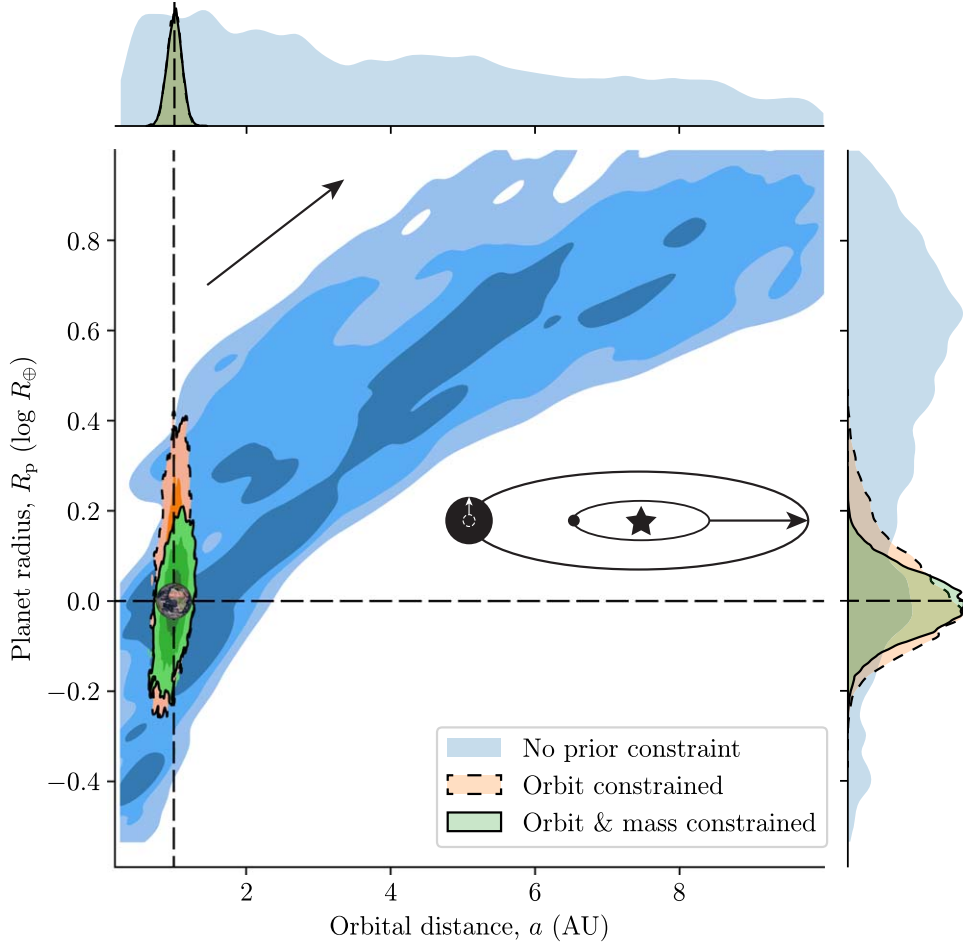


**Figure 2.** Orbital distance and planet radius joint/bivariate (center) and marginal/univariate (top and right side) posterior distributions for different scenarios of prior knowledge and for the vNIR and  $S/N = 20$ . The contours of the 2D posterior distributions denote the  $1\sigma$ ,  $2\sigma$ , and  $3\sigma$  levels, encompassing 68%, 95%, and 99.7% of the observed values, respectively (note that the relevant  $1\sigma$ ,  $2\sigma$ , and  $3\sigma$  levels for a 2D distribution of samples are 39.3%, 86.5%, and 98.9% of the volume, and correspond to the 68%, 95%, and 99.7% for 1D distributions). Earth-like input values are depicted with dashed horizontal and vertical lines. The small image of Earth indicates its position in the diagram. The sketch illustrates the degenerate relationship between increasing orbital distance and increasing planet radius, in yielding an equivalent amount of reflected light. A larger planet orbiting further away from its host star may essentially reflect the same amount of light as a smaller planet but closer to the star. As a result, if the orbit-related parameters are known or constrained, the range of planet radius yielding the same amount of reflected light is necessarily restricted. Retrieval results are given in Table 2.

and  $S/N$ ) on atmospheric retrievals and in determining the best observing strategy in another dedicated study.

Considering the different levels of prior information and the variations in  $S/N$  and spectral coverage, we ran a total of 13 retrieval scenarios and discuss how these scenarios allow us to infer the properties of an observed Earth analog in the next section.

### 3. Results and Discussion

The material below details the value of different types of prior information. First, we explore the impact of priors on determinations of the planetary radius. Next, we highlight how the inference of key parameters is influenced by prior information versus increasing the  $S/N$ .

#### 3.1. Planet Radius Determination

Figure 2 illustrates the degenerate relationship between increasing orbital distance and increasing planetary radius in yielding an equivalent amount of reflected light. Indeed, because the flux received (and reflected) by a planet increases with decreasing the orbital distance and with increasing the

planet radius, a larger planet orbiting further away from its host star may essentially reflect the same amount of light as a smaller planet but closer to the star. This correlation follows directly from the ratio of planetary size to orbital distance in Equation (1). More subtly, Nayak et al. (2017) showed that a similar degenerate relationship exists between the planet phase and radius. Increasing the planet radius may reflect essentially the same amount of light and compensates for a decreasing planet phase (increasing phase angle). Because the geometric albedo ( $A_g$ ) and the phase function ( $\Phi$ ) are physically bound via optical scattering and absorption, measuring the planet-to-star flux ratio while knowing the planetary phase angle and the orbital distance would then ultimately enable inferences of the planet radius (Equation (1)).

A prior determination of the orbit would give constraints on the orbital distance and planetary phase angle at the time of observation. Thus, in such a case, the planet radius required to match the amount of reflected light becomes tightly constrained (orange area in Figure 2). Figure 3 shows posterior constraints on the planetary radius and type as a function of the prior information available for vNIR at  $S/N = 20$  and clearly illustrates this behavior. Without any prior knowledge on the

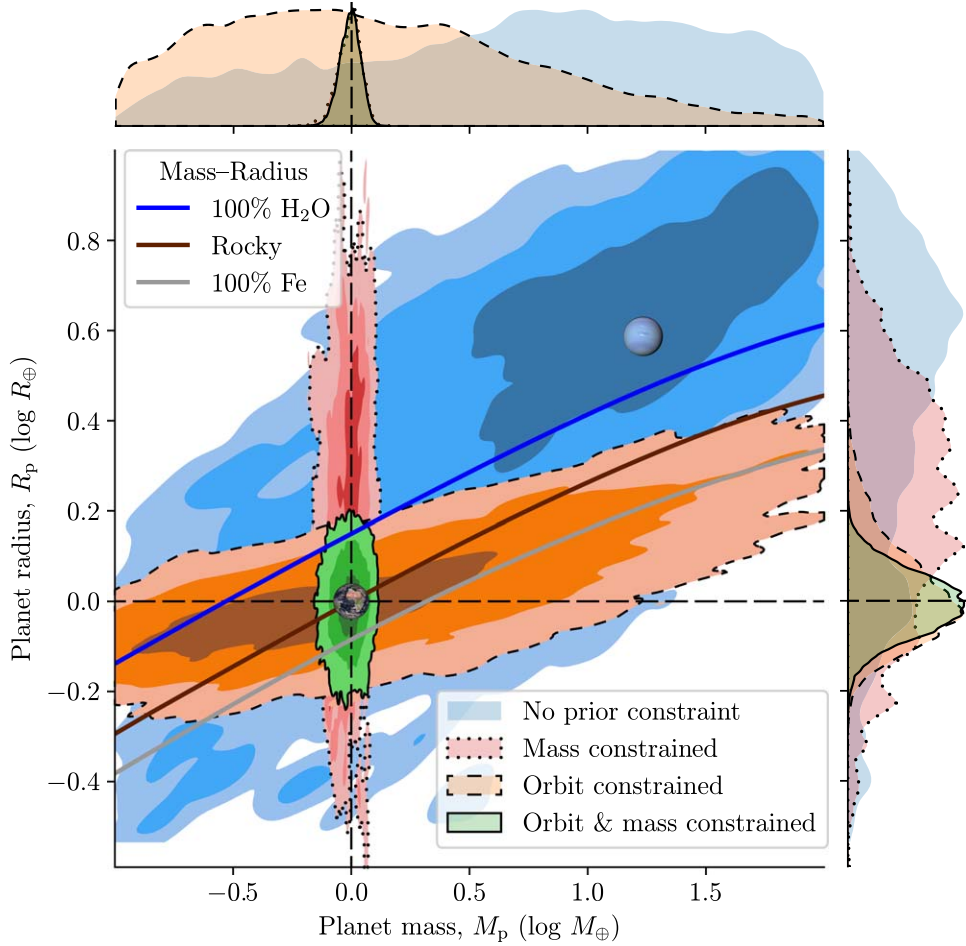


**Figure 3.** Mass–radius diagram (center) and marginal univariate posterior distributions (top and right side) for the different scenarios of prior knowledge and for the vNIR and S/N = 20 case. The contours of the 2D posterior distributions denote the  $1\sigma$ ,  $2\sigma$ , and  $3\sigma$  levels, encompassing 68%, 95%, and 99.7% of the observed values, respectively. Earth-like input values are depicted with dashed horizontal and vertical lines. The small images of Earth and Neptune indicate their positions in the diagram. For comparison, mass–radius relationships representative of different bulk compositions and interior structures are shown (pure H<sub>2</sub>O assuming 1 mbar surface pressure level at 300 K, Earth-like rocky: 32.5% Fe + 67.5% MgSiO<sub>3</sub>, and pure iron; from Zeng et al. 2019 (<https://lweb.cfa.harvard.edu/~lzeng/planetmodels.html#mrrelation>)). Retrieval results are given in Table 2.

retrieved parameters (blue areas in Figure 3), and without any mass–radius relationship assumed, the full prior range for the planet radius is explored ( $\log R_p/R_\oplus = 0.47^{+0.28}_{-0.47}$ , i.e., the radius is confidently constrained to be within 0.99 and 5.63  $R_\oplus$  for the  $1\sigma$  or 68% credible interval), meaning that any radius may satisfactorily reproduce the observed spectrum. As seen from the marginal posterior distribution that weakly peaks above Neptune-sized planets ( $R_\oplus = 3.865 R_\oplus = 0.587 \log R_\oplus$ ), large planets could be mistakenly favored over Earth-sized planets.

Because of the orbit–radius correlation, prior knowledge of the orbit significantly restricts the range of likely radius, i.e., reproducing the observations, yielding accurate radius determination. The radius is confidently constrained to be between 0.81 and 1.34 Earth radius ( $\log R_p/R_\oplus = 0.00^{+0.12}_{-0.09}$  for the  $1\sigma$  or 68% credible interval). The planet is then properly and without ambiguity identified as an Earth-sized planet. Prior knowledge of the orbit also yields a tight radius characterization in all retrieval scenarios conducted, including for different S/N values in the vNIR bandpass (Figure 4). Even for a reduced red bandpass ( $\lambda = [0.87, 1.05] \mu\text{m}$ , with a spectral resolving power  $\text{res} = 140$ ; see Figure 1) and a S/N = 10 (specified at  $\lambda = 0.88 \mu\text{m}$ ), the planet radius is confidently constrained to be between 0.63 and 1.73 Earth radius when the orbit is already determined ( $\log R_p/R_\oplus = -0.02^{+0.25}_{-0.19}$  for the

68% confidence interval, corresponding to  $R_p = 0.96^{+0.77}_{-0.33} R_\oplus$ ), while it is unconstrained ( $R_p = 2.77^{+3.37}_{-1.91} R_\oplus$ ) without prior knowledge (see Figure 6 and Table 5 in Appendix B). Importantly, it shows that these results are not strongly dependent on the wavelength coverage or S/N considered. Note that characterizing the radius this way would reduce important degeneracies involving it and thus help constrain other parameters (Carrión-González et al. 2020).

Because of the already tight constraints on the radius, the mass prior, added to the orbit-related priors, does not offer substantial improvements on the planetary radius constraint, neither for observations in the vNIR ( $\log R_p/R_\oplus = -0.01^{+0.07}_{-0.07}$ , corresponding to  $R_p = 0.98^{+0.17}_{-0.14} R_\oplus$ ; see Figure 3) nor in the red bandpass ( $\log R_p/R_\oplus = -0.03^{+0.23}_{-0.16}$ , corresponding to  $R_p = 0.93^{+0.67}_{-0.29} R_\oplus$ ; see Figure 6 in Appendix B). However, such mass information could prove valuable when attempting to holistically understand the world, as the added mass information helps to constrain bulk properties like density. Here, with both orbit-related and mass priors, the planet is unequivocally identified as rocky. However, results where only the mass is constrained by prior information (red areas in Figures 3 and 4, and Table 2) indicate that knowing only the planet mass would not be sufficient to firmly constrain the

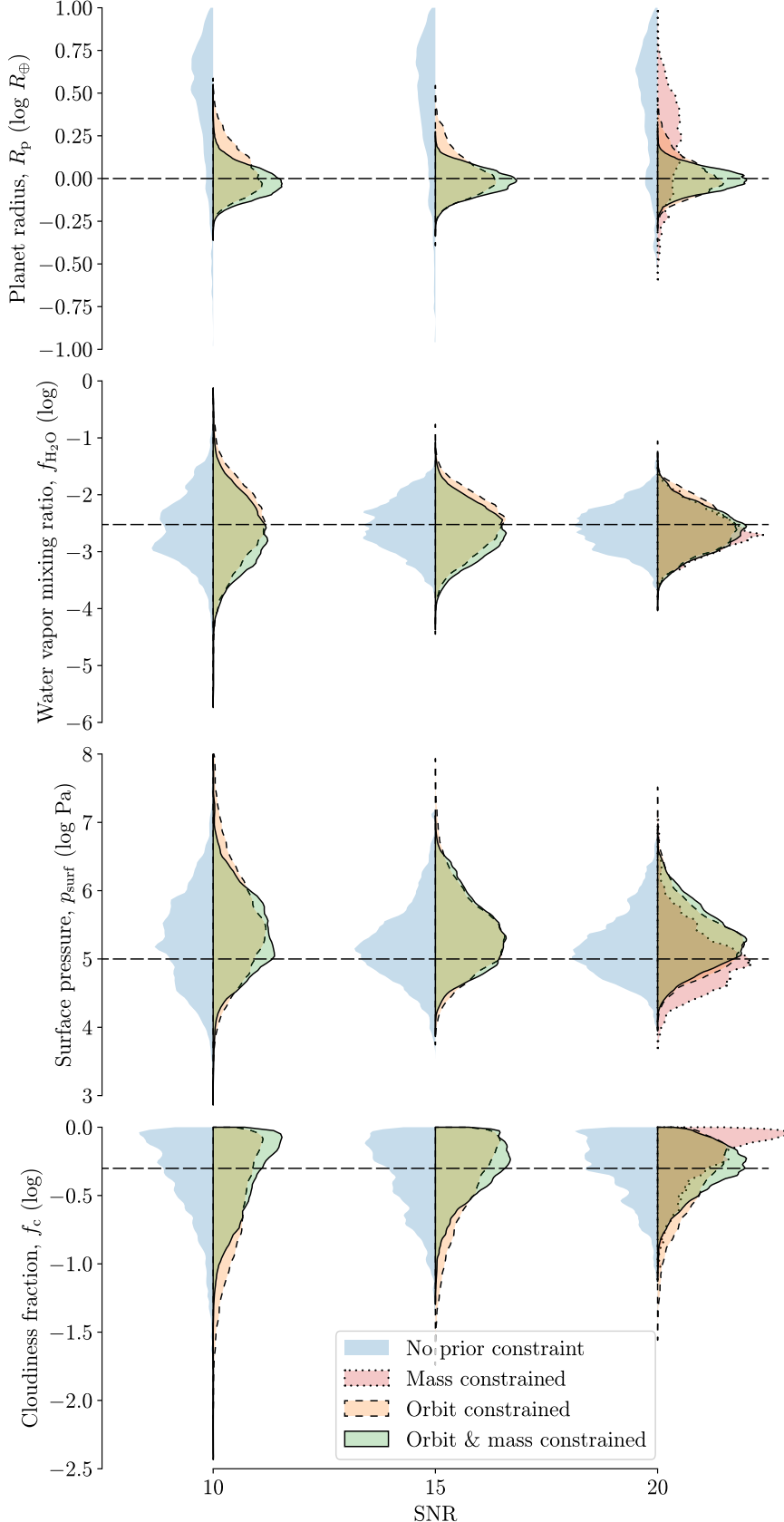


**Figure 4.** Planet radius ( $R_p$ ), water vapor mixing ratio ( $f_{H_2O}$ ), surface pressure ( $p_{surf}$ ), and cloud fraction ( $f_c$ ) posterior distributions for the different levels of color-coded prior knowledge, at different S/N values (10, 15, and 20) in the vNIR. The “mass constrained” case (i.e., where only the mass is constrained; in red) is shown for S/N = 20 only. Earth-like input values are depicted with dashed horizontal lines. The density has been normalized across all kernel density plots such that each have the same area. Apart from the planet radius inference, which is significantly improved by prior knowledge of the orbit, increasing the S/N is more beneficial for atmospheric characterization; as illustrated by the shrinking tails of the posterior distributions and their narrowing toward the fiducial values with increasing S/N (see also Tables 2, 3, and 4 for the retrieval results).

planet radius ( $\log R_p/R_\oplus = 0.22^{+0.25}_{-0.29}$ , corresponding to a planet of 0.84–2.94 Earth radii at the 68% confidence interval) due to the weaker  $M_p$ – $R_p$  correlation, but rules out Neptune-sized planets ( $3.865 R_\oplus$ ) at the 68% credible interval.

### 3.2. Atmospheric Properties and Surface Conditions Inference

The influence of prior observations on the inference of key parameters ( $R_p$ ,  $f_{\text{H}_2\text{O}}$ ,  $p_{\text{surf}}$ , and  $f_c$ ) is shown in Figure 4 for the vNIR, while retrieval results for the full suite of parameters at  $S/N = 20, 15$ , and  $10$  are given in Appendix A, in Tables 2, 3, and 4, respectively. The corresponding posterior distributions obtained for different  $S/N$  are also shown to assess the relative value of adding more  $S/N$  (i.e., integrating longer) against adding more prior observations. For additional details, univariate and bivariate posterior distributions of the full suite of retrieved parameters for observations in the vNIR at  $S/N = 20$ , and for the different scenarios of prior knowledge, are provided as a corner plot in Figure 5 of Appendix A.

Except for the planet radius and regardless of the  $S/N$  value, prior knowledge of the orbit-related parameters and/or of the mass does not significantly improve retrieval accuracy and atmospheric/exoplanet characterization (Figure 4). This contrasts with the idea that “knowledge of a planet’s mass (along with a knowledge of its radius) is essential [...] to interpret spectroscopic features in its atmosphere” (National Academies of Sciences Engineering & Medicine 2018). Only the cloudiness fraction ( $f_c$ ) inference is noticeably refined by prior determination of the mass, and this only when the orbit is already informed: adding the mass prior to the orbit-related knowledge shrinks the tail of the posterior and shifts its peak toward the fiducial value, which allows to constrain  $f_c$  for  $S/N = 15$  (green compared to orange area of the middle and bottom panel of Figure 4 and Table 3).

On the other hand, the top pressure of the cloud deck ( $p_c$ ) inference is only marginally refined when adding the mass prior to the already informed orbit at  $S/N = 10$  (Table 4). Its posterior distribution peaks around the fiducial value for all scenarios and  $p_c$  only becomes “constrained” because the uncertainties are slightly reduced and fall below the 1 log-unit threshold of our inference accuracy classification when adding the mass prior (Appendix A).

To understand the role of the mass prior, recall that planetary mass directly impacts surface gravity, and surface gravity is inversely proportional to the column abundance of molecules above a given pressure. As absorption features are roughly sensitive to the product of the opacity and the column abundance (which sets the atmospheric transmissivity), one might expect that gas mixing ratio constraints would correlate strongly with gravity and mass, such that mass prior information would translate into much-improved atmospheric composition constraints. However, Rayleigh scattering optical depth is directly sensitive to the bulk column abundance of the atmosphere, thereby helping to prevent a degeneracy between planetary mass and atmospheric composition. Observations detecting a Rayleigh scattering slope in the visible thus inform the bulk column abundance and allow constraints on gas mixing ratios without requiring prior mass knowledge. Improving observational quality for spectral features by increasing the  $S/N$  thus yields better constraints on the mixing ratio whereas prior information on the mass does not.

Without measuring the Rayleigh scattering slope—such as for observations in the red bandpass—constraints on

atmospheric composition worsen (e.g., Table 5) because of the degeneracy between planetary mass and atmospheric column abundance. Note that detecting a Rayleigh scattering slope is not critically required to constrain gas mixing ratios absent mass information, as even upper limits on Rayleigh scattering opacity can provide corresponding upper limits on the bulk gas column abundance.

Thus, future direct imaging missions should strive to provide observations at the shortest feasible wavelengths, especially if the likelihood of prior mass information is uncertain or unlikely. This is with the caveat that atmospheric hazes could potentially disrupt the Rayleigh signature. Future work should investigate how assumptions of background gases and hazes, and their Rayleigh scattering, impact the atmospheric characterization-related utility of mass priors.

Alternatively, and while it is always constrained otherwise for  $S/N = 20$  even without prior constraints (Table 2), prior knowledge of the orbit only worsens the inference of the cloudiness fraction. In this scenario, the extension of the posterior distribution’s tail to lower values (orange area of the bottom right panel of Figure 4) results in a 68% confidence interval slightly wider than 0.5 log-units, surpassing our “constrained” threshold (see Appendix A).

Increasing the  $S/N$  systematically improves atmospheric characterization, as discussed in Feng et al. (2018). This is illustrated by the fact that the posterior distributions narrow toward the fiducial values and their tails shrink with increasing  $S/N$  (see also Tables 2, 3, and 4 and the width of the 68% credible intervals). Here, an  $S/N$  of at least 15 is required to constrain the water vapor mixing ratio ( $f_{\text{H}_2\text{O}}$ ) and the surface pressure ( $p_{\text{surf}}$ ) becomes constrained from  $S/N = 20$  (Figure 4 and Appendix A).

Overall, apart from prior knowledge of the orbit that allows for accurate radius determination from reflected-light spectroscopy, these results indicate that orbit and/or mass priors do not significantly improve retrieval efficiency for Earth-like worlds and that increasing the  $S/N$  is much more beneficial to atmospheric characterization.

Note that atmospheres significantly differing from Earth-like worlds, such as those of completely haze/cloud-covered terrestrials or gaseous worlds without a solid surface, might have different behaviors for which the applicability of these results should be further tested. In addition, our constraints may change as the architecture for HWO is refined and as we attain a more comprehensive understanding of the noise characteristics. A yield modeling tool (e.g., Delacroix et al. 2016; Stark et al. 2019; Morgan et al. 2021) could then be upgraded to assess the observing strategies that balance orbit determination against atmospheric characterization in scenarios where mass priors are provided or not.

## 4. Conclusion

The detection and characterization of Earth-like planets orbiting within the habitable zone of Sun-like stars has been set as a major goal for the next decade of planetary science. With it, future missions such as the HWO are being designed. Using rfast in a typical HWO setup, we investigated how prior knowledge of the planet mass and orbit-related parameters will affect the characterization of Earth analogs observed in reflected light.

If the orbit of the planet is known a priori, we found that the planet radius can be accurately retrieved from reflected light

observations, regardless of the S/N or spectral coverage considered here. Combined with prior determination of the planet mass derived from radial velocity measurements, these indirect radius constraints would allow for the firm determination of the planet type and density, thus providing key information to assess its composition, and interior structure, and contextualizing the observations in the frame of coupled interior-atmosphere evolution leading to the observed atmospheric state.

While remaining essential to infer fundamental properties, prior knowledge of the mass alone or combined with orbit-related priors does not significantly improve atmospheric characterization or surface conditions inference. Because Rayleigh scattering optical depth is directly sensitive to the bulk column abundance of the atmosphere, detecting a Rayleigh scattering slope or bounding Rayleigh opacity helps to refine gas mixing ratio inferences without requiring prior mass knowledge. Future direct imaging missions should thus strive to provide observations at the shortest feasible wavelengths, especially if the likelihood of prior mass information is uncertain or unlikely. Overall, and apart from radius determination, increasing the S/N of given observations is more beneficial than adding more prior observations to characterize an exoplanet and infer its atmospheric composition.

### Acknowledgments

A.S. and T.D.R. gratefully acknowledge support from NASA’s Habitable Worlds Program (No. 80NSSC20K0226) and from NASA’s Nexus for Exoplanet System Science Virtual Planetary Laboratory (No. 80NSSC18K0829). T.D.R. also acknowledges support from the Cottrell Scholar Program administered by the Research Corporation for Science Advancement. The authors thank the anonymous reviewer for constructive comments that increased the accessibility of the manuscript.

*Software:* Astropy (Astropy Collaboration et al. 2013, 2018, 2022), corner (Foreman-Mackey 2016), emcee (Foreman-Mackey et al. 2013), matplotlib (Hunter 2007), NumPy (Harris et al. 2020), pandas (The pandas development team 2020), rfast (Robinson & Salvador 2023), seaborn (Waskom 2021).

### Appendix A Retrieval Results for vNIR at Different S/N

To describe atmospheric inference accuracy, we use a detection strength classification similar to Feng et al. (2018). Retrieved parameters can be:

1. Tightly constrained (“TC”—for lin-scale prior ranges only): the width of the 68% confidence interval (i.e., the range of values within  $-1$  and  $+1$  standard deviation,  $\sigma$ , from the mean of a Gaussian distribution) is smaller than  $\pm 10\%$  of the input value;
2. Constrained (“C”): for log-scale prior ranges, the width of the 68% confidence interval is contained within 1 log-unit (i.e., within 1 order of magnitude) for prior ranges spanning at least 5 log-units, and within 0.5 log-units otherwise. For lin-scale prior ranges, the width of the 68% confidence interval is contained within 10% of the full prior range width (Table 1). This is typically the case for posterior distributions with a marked peak without tails toward extreme values.
3. Nonconstrained (“NC”): when none of the above conditions are met. This is typically the case when the posterior distribution is flat across the entire (or nearly entire) prior range, or has a substantial tail toward extreme values.

This classification is only relevant to parameters of flat priors. It is not applicable (“NA”) to parameters known a priori and artificially constrained using a Gaussian-shaped, informative prior centered on the truth value (see “Gaussian prior” column in Table 1).

Tables 2, 3, and 4 provide the retrieval results obtained for the different prior information available for observations conducted in the vNIR at S/N of 20, 15, and 10, respectively, along with the detection strength associated with each retrieved parameter.

Figure 5 illustrates the marginal univariate (along the diagonal) and joint bivariate (off-diagonal) posterior distributions of all retrieved parameters for various scenarios of prior knowledge, based on observations in the vNIR at S/N = 20.

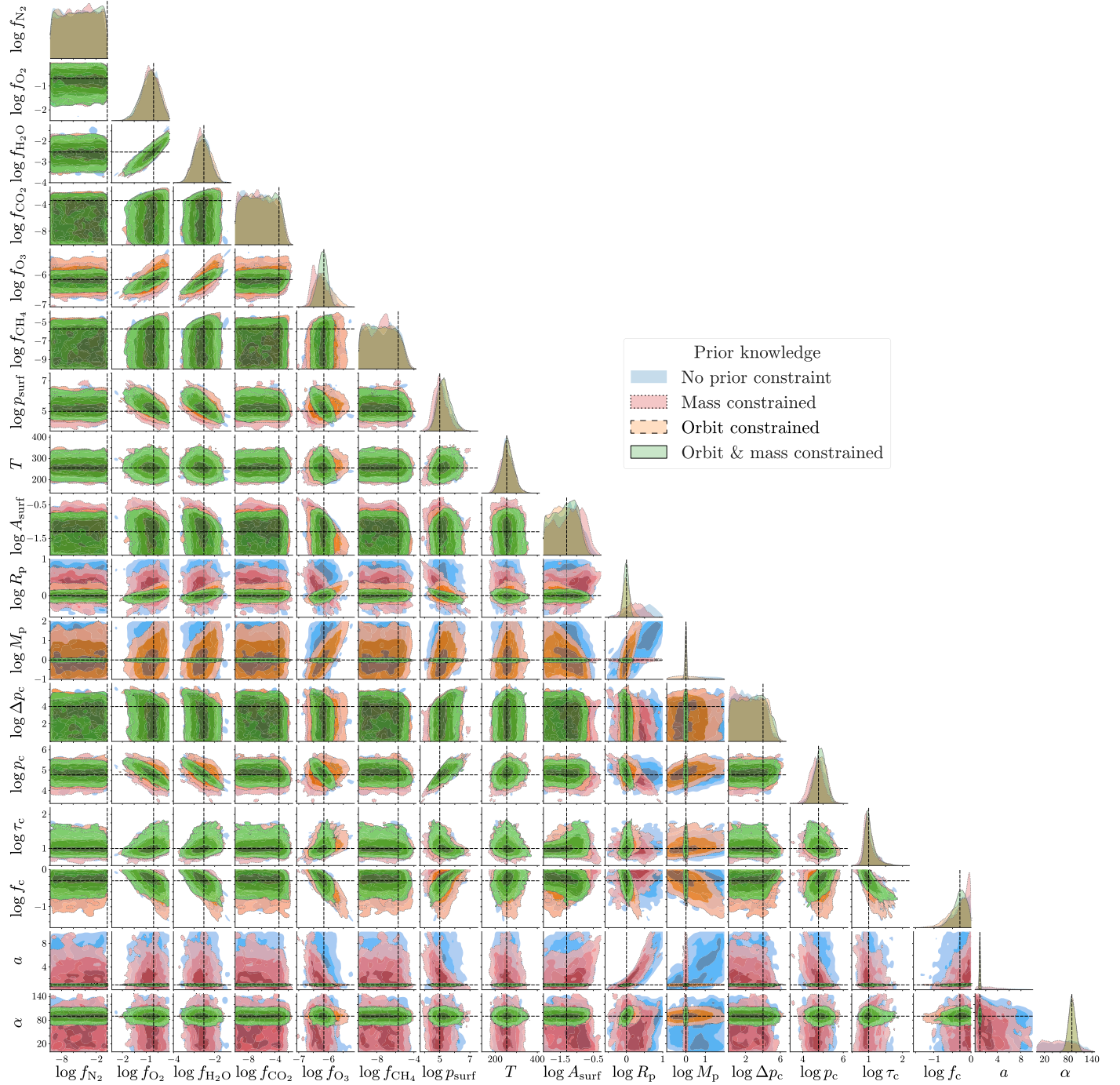


**Figure 5.** Corner plot illustrating the marginal univariate (along the diagonal) and bivariate (off-diagonal) posterior distributions for all retrieved parameters, considering various scenarios of color-coded prior knowledge for observations conducted in the vNIR at S/N = 20 (see Table 2 for quantitative estimates). The contours of the 2D posterior distributions denote the 1 $\sigma$ , 2 $\sigma$ , and 3 $\sigma$  levels, encompassing 68%, 95%, and 99.7% of the observed values, respectively. Earth-like input values are depicted with dashed horizontal and vertical lines.

**Table 2**  
Retrieval Results Comparison and Associated Level of Constraint for the Different Cases of Prior Knowledge Considered for vNIR and S/N = 20

Parameter	Input	No Prior Constraint	Orbit Constrained	Mass and Orbit Constrained	Mass Constrained		
$\log f_{\text{N}_2}$	-0.11	-5.1 $^{+3.28}_{-3.47}$	NC	-4.98 $^{+3.39}_{-3.50}$	NC	-4.81 $^{+3.15}_{-3.37}$	NC
$\log f_{\text{O}_2}$	-0.68	-0.77 $^{+0.35}_{-0.40}$	C	-0.77 $^{+0.37}_{-0.39}$	C	-0.81 $^{+0.35}_{-0.36}$	C
$\log f_{\text{H}_2\text{O}}$	-2.52	-2.57 $^{+0.38}_{-0.41}$	C	-2.58 $^{+0.43}_{-0.40}$	C	-2.62 $^{+0.38}_{-0.39}$	C
$\log f_{\text{CO}_2}$	-3.4	-6.53 $^{+2.47}_{-2.38}$	NC	-6.28 $^{+2.51}_{-2.46}$	NC	-6.2 $^{+2.46}_{-2.55}$	NC
$\log f_{\text{O}_3}$	-6.15	-6.22 $^{+0.30}_{-0.25}$	C	-6.18 $^{+0.33}_{-0.26}$	C	-6.19 $^{+0.15}_{-0.17}$	C
$\log f_{\text{CH}_4}$	-5.7	-7.44 $^{+1.70}_{-1.74}$	NC	-7.46 $^{+1.69}_{-1.70}$	NC	-7.56 $^{+1.72}_{-1.65}$	NC
$\log p_{\text{surf}}$	5.0	5.16 $^{+0.55}_{-0.41}$	C	5.24 $^{+0.47}_{-0.40}$	C	5.29 $^{+0.47}_{-0.39}$	C
$T$	255.0	254.56 $^{+31.44}_{-27.08}$	C	259.52 $^{+28.75}_{-26.66}$	C	258.43 $^{+29.82}_{-26.53}$	C
$\log A_{\text{surf}}$	-1.3	-1.28 $^{+0.38}_{-0.46}$	NC	-1.39 $^{+0.41}_{-0.40}$	NC	-1.35 $^{+0.35}_{-0.43}$	NC
$\log R_p$	0.0	0.47 $^{+0.28}_{-0.47}$	NC	0.0 $^{+0.12}_{-0.09}$	C	-0.01 $^{+0.07}_{-0.07}$	C
$\log M_p$	0.0	0.8 $^{+0.75}_{-1.00}$	NC	0.03 $^{+0.77}_{-0.62}$	NC	-0.01 $^{+0.04}_{-0.05}$	NA
$\log \Delta p_c$	4.0	2.33 $^{+1.74}_{-1.56}$	NC	2.59 $^{+1.80}_{-1.76}$	NC	2.69 $^{+1.66}_{-1.84}$	NC
$\log p_c$	4.78	4.81 $^{+0.34}_{-0.33}$	C	4.88 $^{+0.31}_{-0.33}$	C	4.87 $^{+0.27}_{-0.28}$	C
$\log \tau_c$	1.0	1.0 $^{+0.23}_{-0.12}$	C	1.01 $^{+0.19}_{-0.11}$	C	1.0 $^{+0.17}_{-0.10}$	C
$\log f_c$	-0.3	-0.26 $^{+0.19}_{-0.29}$	C	-0.32 $^{+0.20}_{-0.32}$	NC	-0.29 $^{+0.16}_{-0.20}$	C
$a$	1.0	3.68 $^{+3.63}_{-2.47}$	NC	1.0 $^{+0.10}_{-0.10}$	NA	1.0 $^{+0.10}_{-0.11}$	NA
$\alpha$	90.0	66.28 $^{+37.97}_{-45.75}$	NC	90.14 $^{+8.61}_{-8.89}$	NA	90.16 $^{+9.17}_{-8.55}$	NA

**Note.** For log-scale prior ranges, the parameters are constrained (“C”) when the width of the 68% confidence interval (corresponding to the interval between the mean value  $-1$  and  $+1$  standard deviation) is included within 1 log-unit (i.e., within 1 order of magnitude) for prior ranges spanning at least 5 log-units and within 0.5 log-units otherwise. For lin-scale prior ranges, parameters are constrained (“C”) when the width of the 68% confidence interval is smaller than 10% of the full prior range width, and tightly constrained (“TC”) when smaller than  $\pm 10\%$  of the input value. Parameters are nonconstrained (“NC”) otherwise, corresponding to either flat posterior distributions across the entire (or nearly) prior range or to posterior distributions with marked peaks but also substantial tails toward extreme values. Detection strength is not applicable (“NA”) for parameters known a priori (i.e., Gaussian prior).

**Table 3**  
Retrieval Results Comparison and Associated Level of Constraint for the Different Cases of Prior Knowledge Considered for vNIR and S/N = 15

Parameter	Input	No Prior Constraint	Orbit Constrained	Mass and Orbit Constrained			
$\log f_{\text{N}_2}$	-0.11	-4.81 $^{+3.22}_{-3.35}$	NC	-5.19 $^{+3.36}_{-3.32}$	NC	-4.98 $^{+3.34}_{-3.38}$	NC
$\log f_{\text{O}_2}$	-0.68	-0.76 $^{+0.41}_{-0.52}$	C	-0.77 $^{+0.42}_{-0.53}$	C	-0.88 $^{+0.44}_{-0.52}$	C
$\log f_{\text{H}_2\text{O}}$	-2.52	-2.55 $^{+0.47}_{-0.45}$	C	-2.52 $^{+0.46}_{-0.51}$	C	-2.66 $^{+0.46}_{-0.47}$	C
$\log f_{\text{CO}_2}$	-3.4	-5.83 $^{+2.38}_{-2.88}$	NC	-6.27 $^{+2.59}_{-2.52}$	NC	-6.19 $^{+2.54}_{-2.59}$	NC
$\log f_{\text{O}_3}$	-6.15	-6.2 $^{+0.36}_{-0.30}$	C	-6.16 $^{+0.35}_{-0.30}$	C	-6.21 $^{+0.19}_{-0.21}$	C
$\log f_{\text{CH}_4}$	-5.7	-7.24 $^{+1.70}_{-1.82}$	NC	-7.29 $^{+1.71}_{-1.82}$	NC	-7.48 $^{+1.74}_{-1.72}$	NC
$\log p_{\text{surf}}$	5.0	5.17 $^{+0.56}_{-0.46}$	NC	5.33 $^{+0.58}_{-0.49}$	NC	5.34 $^{+0.57}_{-0.47}$	NC
$T$	255.0	256.76 $^{+37.68}_{-34.37}$	C	257.52 $^{+42.33}_{-36.10}$	C	259.35 $^{+42.71}_{-35.89}$	C
$\log A_{\text{surf}}$	-1.3	-1.22 $^{+0.44}_{-0.46}$	NC	-1.38 $^{+0.42}_{-0.42}$	NC	-1.28 $^{+0.35}_{-0.45}$	NC
$\log R_p$	0.0	0.48 $^{+0.30}_{-0.45}$	NC	0.01 $^{+0.13}_{-0.10}$	C	-0.02 $^{+0.08}_{-0.08}$	C
$\log M_p$	0.0	0.92 $^{+0.71}_{-1.05}$	NC	0.13 $^{+0.90}_{-0.73}$	NC	-0.0 $^{+0.04}_{-0.05}$	NA
$\log \Delta p_c$	4.0	2.65 $^{+1.63}_{-1.74}$	NC	2.63 $^{+1.70}_{-1.74}$	NC	2.58 $^{+1.71}_{-1.74}$	NC
$\log p_c$	4.78	4.8 $^{+0.41}_{-0.41}$	C	4.89 $^{+0.40}_{-0.40}$	C	4.89 $^{+0.35}_{-0.35}$	C
$\log \tau_c$	1.0	1.01 $^{+0.33}_{-0.16}$	C	1.02 $^{+0.24}_{-0.14}$	C	1.0 $^{+0.21}_{-0.13}$	C
$\log f_c$	-0.3	-0.31 $^{+0.21}_{-0.36}$	NC	-0.33 $^{+0.23}_{-0.38}$	NC	-0.28 $^{+0.18}_{-0.24}$	C
$a$	1.0	3.68 $^{+3.71}_{-2.53}$	NC	1.0 $^{+0.10}_{-0.10}$	NA	1.0 $^{+0.10}_{-0.10}$	NA
$\alpha$	90.0	63.0 $^{+42.09}_{-44.11}$	NC	89.98 $^{+8.82}_{-9.01}$	NA	89.66 $^{+8.51}_{-8.90}$	NA

**Table 4**

Retrieval Results Comparison and Associated Level of Constraint for the Different Cases of Prior Knowledge Considered for vNIR and S/N = 10

Parameter	Input	No Prior Constraint	Orbit Constrained	Mass and Orbit Constrained
$\log f_{\text{N}_2}$	-0.11	-4.97 $^{+3.18}_{-3.50}$	NC	-5.03 $^{+3.17}_{-3.36}$
$\log f_{\text{O}_2}$	-0.68	-1.02 $^{+0.59}_{-0.89}$	NC	-0.98 $^{+0.61}_{-0.98}$
$\log f_{\text{H}_2\text{O}}$	-2.52	-2.6 $^{+0.65}_{-0.55}$	NC	-2.51 $^{+0.63}_{-0.67}$
$\log f_{\text{CO}_2}$	-3.4	-6.1 $^{+2.90}_{-2.57}$	NC	-6.14 $^{+2.88}_{-2.68}$
$\log f_{\text{O}_3}$	-6.15	-6.26 $^{+0.42}_{-0.31}$	C	-6.1 $^{+0.41}_{-0.39}$
$\log f_{\text{CH}_4}$	-5.7	-7.42 $^{+1.82}_{-1.76}$	NC	-7.27 $^{+1.91}_{-1.88}$
$\log p_{\text{surf}}$	5.0	5.28 $^{+0.70}_{-0.70}$	NC	5.46 $^{+0.79}_{-0.68}$
$T$	255.0	262.43 $^{+64.32}_{-55.46}$	NC	264.67 $^{+68.99}_{-56.85}$
$\log A_{\text{surf}}$	-1.3	-1.17 $^{+0.47}_{-0.55}$	NC	-1.3 $^{+0.44}_{-0.45}$
$\log R_p$	0.0	0.5 $^{+0.26}_{-0.45}$	NC	0.03 $^{+0.16}_{-0.12}$
$\log M_p$	0.0	0.95 $^{+0.71}_{-1.00}$	NC	0.48 $^{+0.92}_{-0.87}$
$\log \Delta p_c$	4.0	2.55 $^{+1.93}_{-1.84}$	NC	2.53 $^{+2.01}_{-1.76}$
$\log p_c$	4.78	4.75 $^{+0.55}_{-0.58}$	NC	4.93 $^{+0.57}_{-0.58}$
$\log \tau_c$	1.0	1.05 $^{+0.49}_{-0.22}$	C	1.07 $^{+0.54}_{-0.22}$
$\log f_c$	-0.3	-0.32 $^{+0.24}_{-0.40}$	NC	-0.47 $^{+0.33}_{-0.47}$
$a$	1.0	3.84 $^{+3.46}_{-2.78}$	NC	0.99 $^{+0.10}_{-0.10}$
$\alpha$	90.0	67.34 $^{+42.43}_{-44.39}$	NC	90.13 $^{+8.67}_{-9.15}$

## Appendix B Applicability to Other Spectral Coverages

Atmospheric and surface properties inference and detection strengths are sensitive to the spectral region observed and to the S/N (e.g., von Paris et al. 2013; Feng et al. 2018; Damiano et al. 2020; Damiano & Hu 2022; Konrad et al. 2022; Alei et al. 2022a; Robinson & Salvador 2023; Damiano et al. 2023; Latouf et al. 2023a, 2023b; Young et al. 2024; Mettler et al. 2024). While we will specifically address the influence of the spectral coverage combined with the S/N on atmospheric retrievals of Earth analogs in another study, Figure 6 and Table 5 show the mass–radius posterior distributions and the retrieval results and detection strengths obtained for the different prior information scenarios for observations conducted in a narrower “red” bandpass ( $\lambda = [0.87, 1.05] \mu\text{m}$ , with

a spectral resolving power  $\text{res} = 140$ ; see Figure 1) and a S/N = 10 (specified at  $\lambda = 0.88 \mu\text{m}$ ). They demonstrate that our conclusions are independent of the spectral coverage considered. Indeed, for observations in the red bandpass at S/N = 10, a prior determination of the orbit-related parameters (i.e., orbital distance and phase angle; orange areas of Figure 6) yields tight constraints on the planet radius. It is confidently constrained to be between 0.63 and 1.73 Earth radius ( $\log R_p/R_\oplus = -0.02^{+0.25}_{-0.19}$  for the 68% confidence interval, compared to  $\log R_p/R_\oplus = 0.44^{+0.35}_{-0.51}$  without any prior knowledge). On the other hand, the mass prior, when added to the orbit-related priors, does not offer substantial improvements on the planetary radius constraint ( $\log R_p/R_\oplus = -0.03^{+0.23}_{-0.16}$ , corresponding to  $R_p = 0.93^{+0.67}_{-0.29} R_\oplus$ ; green areas of Figure 6), nor on the inference of other parameters (Table 5).

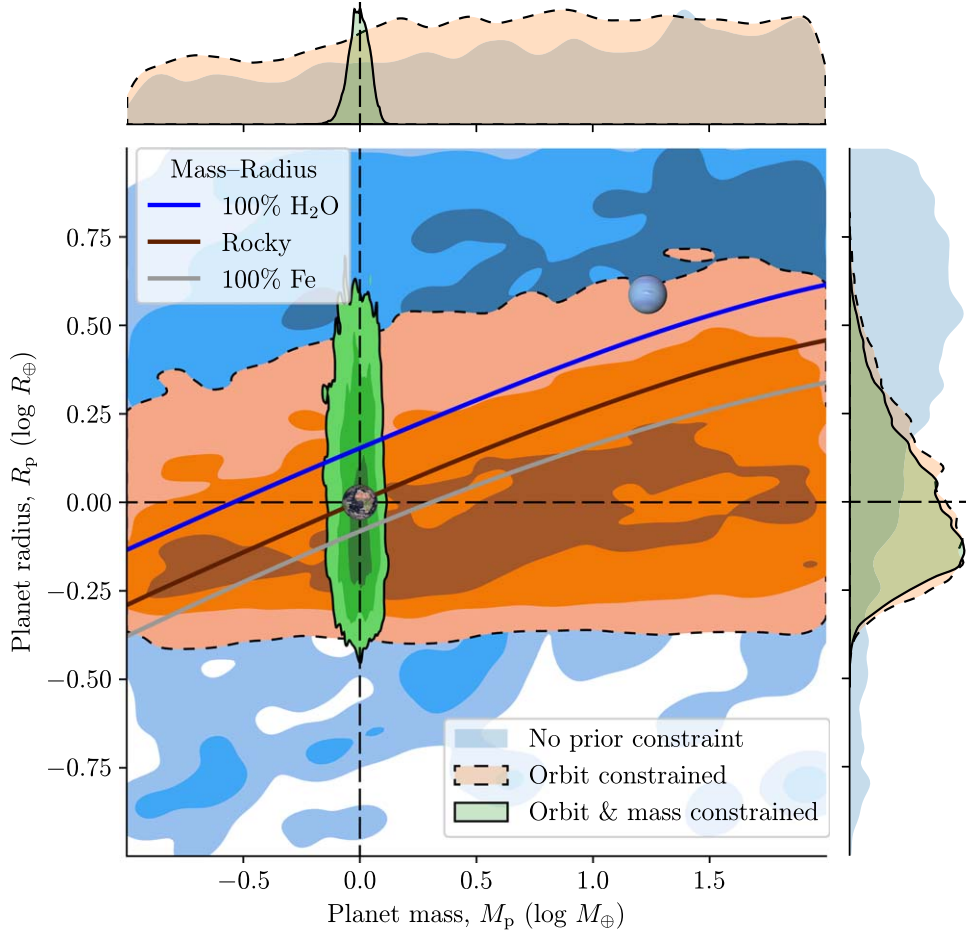


**Figure 6.** Mass–radius diagram (center) and marginal univariate posterior distributions (top and right side) for the different scenarios of prior knowledge (same as Figure 3) considering a narrower spectral bandpass centered on “red” wavelengths ( $\lambda = [0.87, 1.05] \mu\text{m}$ , res = 140; see Figure 1) and  $S/N = 10$ . The contours of the 2D posterior distributions denote the  $1\sigma$ ,  $2\sigma$ , and  $3\sigma$  levels, encompassing 68%, 95%, and 99.7% of the observed values, respectively. Earth-like input values are depicted with dashed horizontal and vertical lines. The small images of Earth and Neptune indicate their positions in the diagram. For comparison, mass–radius relationships representative of different bulk compositions and interior structures are shown (pure  $\text{H}_2\text{O}$  assuming 1 mbar surface pressure level at 300 K, Earth-like rocky: 32.5% Fe + 67.5%  $\text{MgSiO}_3$ , and pure iron; from Zeng et al. 2019). Retrieval results are given in Table 5.

**Table 5**

Retrieval Results Comparison and Associated Level of Constraint for the Different Cases of Prior Knowledge Considered for the Red Bandpass (Figure 1) and  $S/N = 10$

Parameter	Input	No Prior Constraint	Orbit Constrained	Mass and Orbit Constrained
$\log f_{\text{N}_2}$	-0.11	$-4.54^{+3.34}_{-3.62}$	NC	$-4.98^{+3.29}_{-3.36}$
$\log f_{\text{O}_2}$	-0.68	$-5.3^{+3.38}_{-3.41}$	NC	$-5.47^{+3.60}_{-3.10}$
$\log f_{\text{H}_2\text{O}}$	-2.52	$-1.94^{+1.13}_{-1.59}$	NC	$-1.64^{+1.03}_{-1.23}$
$\log f_{\text{CO}_2}$	-3.4	$-5.49^{+3.28}_{-3.26}$	NC	$-5.02^{+3.23}_{-3.37}$
$\log f_{\text{O}_3}$	-6.15	$-6.13^{+2.92}_{-2.71}$	NC	$-6.04^{+2.64}_{-2.62}$
$\log f_{\text{CH}_4}$	-5.7	$-6.83^{+2.42}_{-2.18}$	NC	$-6.44^{+2.34}_{-2.39}$
$\log p_{\text{surf}}$	5.0	$4.88^{+1.44}_{-0.94}$	NC	$4.92^{+0.88}_{-0.75}$
$T$	255.0	$277.09^{+95.47}_{-66.23}$	NC	$286.48^{+92.67}_{-70.65}$
$\log A_{\text{surf}}$	-1.3	$-0.62^{+0.44}_{-0.73}$	NC	$-0.62^{+0.43}_{-0.67}$
$\log R_p$	0.0	$0.44^{+0.35}_{-0.51}$	NC	$-0.02^{+0.25}_{-0.19}$
$\log M_p$	0.0	$0.82^{+0.84}_{-1.06}$	NC	$0.7^{+0.88}_{-1.00}$
$\log \Delta p_c$	4.0	$2.52^{+1.63}_{-1.68}$	NC	$2.29^{+1.66}_{-1.54}$
$\log p_c$	4.78	$2.79^{+1.65}_{-1.83}$	NC	$2.68^{+1.67}_{-1.83}$
$\log \tau_c$	1.0	$-0.07^{+1.95}_{-1.99}$	NC	$-0.0^{+1.96}_{-2.05}$
$\log f_c$	-0.3	$-1.32^{+1.04}_{-1.19}$	NC	$-1.41^{+1.05}_{-1.05}$
$a$	1.0	$3.34^{+3.83}_{-2.37}$	NA	$1.0^{+0.10}_{-0.10}$
$\alpha$	90.0	$65.79^{+47.86}_{-42.59}$	NC	$89.94^{+9.19}_{-9.60}$
			NA	$90.14^{+8.33}_{-8.73}$
			NA	$1.0^{+0.10}_{-0.09}$
			NA	$1.0^{+0.10}_{-0.09}$

## ORCID iDs

- Arnaud Salvador <https://orcid.org/0000-0001-8106-6164>  
 Tyler D. Robinson <https://orcid.org/0000-0002-3196-414X>  
 Jonathan J. Fortney <https://orcid.org/0000-0002-9843-4354>  
 Mark S. Marley <https://orcid.org/0000-0002-5251-2943>

## References

- Akeson, R., Armus, L., Bachelet, E., et al. 2019, arXiv:[1902.05569](https://arxiv.org/abs/1902.05569)  
 Alei, E., Konrad, B. S., Angerhausen, D., et al. 2022a, *A&A*, **665**, A106  
 Alei, E., Konrad, B. S., Mollière, P., et al. 2022b, *Proc. SPIE*, **12180**, 121803L  
 Astropy Collaboration, Price-Whelan, A. M., Lim, P. L., et al. 2022, *ApJ*, **935**, 167  
 Astropy Collaboration, Price-Whelan, A. M., Sipőcz, B. M., et al. 2018, *AJ*, **156**, 123  
 Astropy Collaboration, Robitaille, T. P., Tollerud, E. J., et al. 2013, *A&A*, **558**, A33  
 Benneke, B., & Seager, S. 2012, *ApJ*, **753**, 100  
 Benneke, B., & Seager, S. 2013, *ApJ*, **778**, 153  
 Carrión-González, Ó., García Muñoz, A., Cabrera, J., et al. 2020, *A&A*, **640**, A136  
 Carrión-González, Ó., García Muñoz, A., Santos, N. C., et al. 2021, *A&A*, **655**, A92  
 Damiano, M., & Hu, R. 2020, *AJ*, **159**, 175  
 Damiano, M., & Hu, R. 2021, *AJ*, **162**, 200  
 Damiano, M., & Hu, R. 2022, *AJ*, **163**, 299  
 Damiano, M., Hu, R., & Hildebrandt, S. R. 2020, *AJ*, **160**, 206  
 Damiano, M., Hu, R., & Mennesson, B. 2023, *AJ*, **166**, 157  
 Delacroix, C., Savransky, D., Garrett, D., Lowrance, P., & Morgan, R. 2016, *Proc. SPIE*, **9911**, 991119  
 Dulz, S. D., Plavchan, P., Crepp, J. R., et al. 2020, *ApJ*, **893**, 122  
 Feng, Y. K., Robinson, T. D., Fortney, J. J., et al. 2018, *AJ*, **155**, 200  
 Foreman-Mackey, D. 2016, *JOSS*, **1**, 24  
 Foreman-Mackey, D., Hogg, D. W., Lang, D., & Goodman, J. 2013, *PASP*, **125**, 306  
 Fortney, J. J., Barstow, J. K., & Madhusudhan, N. 2021, *ExoFrontiers* (Bristol: IOP Publishing), **10**  
 Gaudi, B. S., Seager, S., Mennesson, B., et al. 2018, *NatAs*, **2**, 600  
 Gaudi, B. S., Seager, S., Mennesson, B., et al. 2020, arXiv:[2001.06683](https://arxiv.org/abs/2001.06683)  
 Greene, T. P., Line, M. R., Montero, C., et al. 2016, *ApJ*, **817**, 17  
 Guyon, O., Pluzhnik, E. A., Kuchner, M. J., Collins, B., & Ridgway, S. T. 2006, *ApJS*, **167**, 81  
 Guyon, O., Eisner, J. A., Angel, R., et al. 2013, *ApJ*, **767**, 11  
 Harness, A., Shaklan, S., Willems, P., et al. 2021, *JATIS*, **7**, 21207  
 Harris, C. R., Millman, K. J., van der Walt, S. J., et al. 2020, *Natur*, **585**, 357  
 Horak, H. G., & Little, S. J. 1965, *ApJS*, **11**, 373  
 Horning, A., Morgan, R., & Nielson, E. 2019, *Proc. SPIE*, **11117**, 111171C  
 Hunter, J. D. 2007, *CSE*, **9**, 90  
 Juanola-Parramon, R., Zimmerman, N. T., Pueyo, L., et al. 2022, *JATIS*, **8**, 34001  
 Kasting, J. F., Whitmire, D. P., & Reynolds, R. T. 1993, *Icar*, **101**, 108  
 Konrad, B. S., Alei, E., Quanz, S. P., et al. 2022, *A&A*, **664**, A23  
 Lacy, B., Shlivko, D., & Burrows, A. 2019, *AJ*, **157**, 132  
 Latouf, N., Mandell, A. M., Villanueva, G. L., et al. 2023a, *AJ*, **166**, 129  
 Latouf, N., Mandell, A. M., Villanueva, G. L., et al. 2023b, *AJ*, **167**, 27  
 Lovis, C., Fischer, D. A., & Dotson, R. 2010, Radial Velocity Techniques for Exoplanets (Tucson, AZ: Univ. of Arizona Press), 27, <http://www.jstor.org/stable/j.ctt1814jx6.8>  
 Lupu, R. E., Marley, M. S., Lewis, N., et al. 2016, *AJ*, **152**, 217  
 Lustig-Yaeger, J., Meadows, V. S., Crisp, D., Line, M. R., & Robinson, T. D. 2023, *PSJ*, **4**, 170  
 Madhusudhan, N. 2018, in *Handbook of Exoplanets*, ed. H. J. Deeg & J. A. Belmonte (Cham: Springer), **2153**  
 Madhusudhan, N. 2019, *ARA&A*, **57**, 617  
 Mennesson, B., Juanola-Parramon, R., Nemati, B., et al. 2020, arXiv:[2008.05624](https://arxiv.org/abs/2008.05624)  
 Mettler, J.-N., Konrad, B. S., Quanz, S. P., & Helled, R. 2024, *ApJ*, **963**, 24  
 Morgan, R. M., Savransky, D., Turmon, M. J., et al. 2021, *JATIS*, **7**, 21220  
 Morley, C. V., Fortney, J. J., Marley, M. S., et al. 2015, *ApJ*, **815**, 110  
 National Academies of Sciences Engineering and Medicine 2018, *Exoplanet Science Strategy* (Washington, DC: The National Academies Press)  
 National Academies of Sciences Engineering and Medicine 2023a, *Pathways to Discovery in Astronomy and Astrophysics for the 2020s* (Washington, DC: The National Academies Press)  
 National Academies of Sciences, Engineering, and Medicine 2023b, *Origins, Worlds, and Life: A Decadal Strategy for Planetary Science and Astrobiology 2023-2032* (Washington, DC: The National Academies Press),  
 Nayak, M., Lupu, R., Marley, M. S., et al. 2017, *PASP*, **129**, 034401  
 Plavchan, P., Latham, D., Gaudi, S., et al. 2015, arXiv:[1503.01770](https://arxiv.org/abs/1503.01770)  
 Roberge, A., & Moustakas, L. A. 2018, *NatAs*, **2**, 605  
 Robinson, T. D., Meadows, V. S., & Crisp, D. 2010, *ApJL*, **721**, L67  
 Robinson, T. D., & Salvador, A. 2023, *PSJ*, **4**, 10  
 Robinson, T. D., Stapelfeldt, K. R., & Marley, M. S. 2016, *PASP*, **128**, 025003  
 Seager, S., & Deming, D. 2010, *ARA&A*, **48**, 631  
 Smith, A. J. R. W., Feng, Y. K., Fortney, J. J., et al. 2020, *AJ*, **159**, 36  
 Stark, C. C., Belikov, R., Bolcar, M. R., et al. 2019, *JATIS*, **5**, 24009  
 Susemehl, N., Mandell, A. M., Villanueva, G. L., et al. 2023, *AJ*, **166**, 86  
 The LUVOIR Team 2019, arXiv:[1912.06219](https://arxiv.org/abs/1912.06219)  
 The pandas development team 2020, *pandas-dev/pandas: Pandas*, v1.5.3, Zenodo, doi: [10.5281/zenodo.3509134](https://doi.org/10.5281/zenodo.3509134)  
 Trauger, J. T., & Traub, W. A. 2007, *Natur*, **446**, 771  
 von Paris, P., Hedelt, P., Selsis, F., Schreier, F., & Trautmann, T. 2013, *A&A*, **551**, A120  
 Wang, F., Fujii, Y., & He, J. 2022, *ApJ*, **931**, 48  
 Waskom, M. L. 2021, *JOSS*, **6**, 3021  
 Welbanks, L., & Madhusudhan, N. 2019, *AJ*, **157**, 206  
 Williams, D. M., & Gaidos, E. 2008, *Icar*, **195**, 927  
 Young, A. V., Crouse, J., Arney, G., et al. 2024, *PSJ*, **5**, 7  
 Zeng, L., Jacobsen, S. B., Sasselov, D. D., et al. 2019, *PNAS*, **116**, 9723